The Meteoritical Society

Meteoritics & Planetary Science 46, Nr 11, 1619–1629 (2011)
doi: 10.1111/j.1945-5100.2011.01249.x

Shock experiments on anhydrite and new constraints on the impact-induced SO_x release at the K-Pg boundary

Clemens PRESCHER[1], Falko LANGENHORST[1,2*], Ulrich HORNEMANN[3], and Alexander DEUTSCH[4]

[1]Bayerisches Geoinstitut (BGI), Universität Bayreuth, D-95440 Bayreuth, Germany
[2]Present address: Institut für Geowissenschaften, Friedrich-Schiller-Universität Jena, Burgweg 11, D-07749 Jena, Germany
[3]Fraunhofer-Institut für Kurzzeitdynamik, Ernst-Mach Institut (EMI), Eckerstraße 4, D-79104 Freiburg, Germany
[4]Institut für Planetologie (IfP), Westfälische Wilhelms-Universität Münster, Wilhelm-Klemm-Str. 10, D-48149 Münster, Germany
*Corresponding author. E-mail: falko.langenhorst@uni-jena.de

(Received 16 April 2011; revision accepted 06 August 2011)

Abstract–We have performed six shock experiments at nominal peak-shock pressures of 12.5, 20, 33, 46.5, 64, and 85 GPa using polycrystalline anhydrite discs embedded in ARMCO-Fe sample containers and the shock reverberation technique. The recovered samples were analyzed using X-ray powder diffraction and transmission electron microscopy (TEM). The X-ray diffraction patterns recorded on all samples are compatible with the anhydrite structure; extra-peaks have not been observed. Peak intensities decrease and peak broadening increases progressively in the pressure range from 0 to 46.5 GPa. At higher pressures, peak broadening diminishes and the X-ray diffraction pattern of the 85 GPa sample resembles essentially that of unshocked, well-crystallized anhydrite. Related structural changes at the nanoscale include in the pressure regime up to 20 GPa "cold" deformation phenomena such as cracks and deformation twins. Dislocation density increases up to 33 GPa and the strain increases up to 46.5 GPa. In the pressure range from 46.5 to 85 GPa, high postshock temperatures caused annealing of the deformation features. Increasing density and size of voids in the anhydrite samples shocked at 64 and 85 GPa indicate partial decomposition of anhydrite. Recalculation of the peak-shock pressure in the experiments to a more realistic natural loading path indicates the onset of degassing of anhydrite in the pressure range of 30–41 GPa.

INTRODUCTION

The K-Pg (Cretaceous–Paleogene) mass extinction is now widely accepted to have been induced to a large extent by the release of vast amounts of SO_x gases due to the Chicxulub bolide impact into a carbonate/sulfate platform at Yucatán Peninsula, Mexico (for a recent review see Schulte et al. 2010). In detail, however, the related mechanisms are not well understood, mainly because the amount of gases released, and their effect on global climate (e.g., Pierazzo et al. 2003; Kring 2007) are not well constrained. It is, therefore, essential to investigate the shock behavior of sulfates experimentally and theoretically; the results may also be of interest in the context of Martian evolution (e.g., Wiseman et al. 2010).

Decomposition of shocked carbonates is well documented in nature (e.g., Osinski and Spray 2001; Deutsch and Langenhorst 2007), by experiments (Langenhorst et al. 2002; Zhang and Sekine 2007; Bell 2010), modeling (Ivanov and Deutsch 2002; Ivanov et al. 2002), and recarbonation of the resultant lime was experimentally examined in detail (Agrinier et al. 2001). However, similar data for shocked sulfates are rather sparse (Skála et al. 2004). The shock behavior of anhydrite (orthorhombic $CaSO_4$), the dominating sulfate in the target region of the Chixculub impact event, was mainly inferred from thermodynamic considerations (Chen et al. 1994; Ivanov et al. 1996, 2004; Pope et al. 1997; Yang and Ahrens 1998; Gupta et al. 2001), but lacks postmortem confirmation by mineralogical

Table 1. Parameters of shock experiments performed with anhydrite powder at the Ernst-Mach-Institut, Freiburg, Germany.

Nominal pressure (GPa)	Experiment #	Cover plate thickness (mm)	Flyer plate thickness (mm)	High explosive
85	9455	5	2	Octogen
64	9456	5	3.3	Octogen
46.5	9457	5	3	Composition B
33	9458	10	4	Composition B
20	9459	5	4	TNT
12.5	9460	10	5	TNT

investigation of recovered material from shock experiments. In a recent abstract, however, gas release from gypsum (monoclinic, $CaSO_4{\cdot}2H_2O$) in laser shock experiments was documented by specification of the SO_3/SO_2 ratio using quadrupole mass spectrometry (Ohno et al. 2010).

Pressure estimates for shock-induced incipient and complete decomposition of anhydrite vary widely. First calculations on the basis of energetic considerations resulted in pressures of approximately 80 GPa and approximately 160 GPa for incipient and complete decomposition, respectively (Badjukov et al. 1995; Ivanov et al. 1996). Later, the "entropy criterion" for vaporization (Zel'dovich and Raizer 2002) was introduced into calculations by Gupta et al. (2001), yielding shock pressures for incipient and complete vaporization of 32 ± 2.5 GPa and 122 ± 13 GPa, respectively. As gaseous SO_2/SO_3 have very high molar entropies and volumes compared with the solid mineral anhydrite, shock-induced decomposition of minerals occurs during and after unloading from peak-shock pressures, whereby postshock temperatures essentially determine the degree of devolatilization. As documented by Kondo and Ahrens (1983) in shock experiments with gypsum, the problem is complicated by localized spots of peak temperatures exceeding the calculated Hugoniot temperatures up to a factor of 10. In the natural case, porosity of the evaporate layers in the target plays a prominent role, as high porosity will result in high shock and postshock temperatures at even relatively low shock pressures (e.g., Wünnemann et al. 2008).

Investigations on recovered shock-loaded anhydrite samples mostly employed X-ray diffraction methods (Schmitt and Hornemann 1998; Langenhorst et al. 2003; Skála et al. 2004, 2005). Skála et al. (2004) reported, in addition, some scanning electron microscopy (SEM) and transmission electron microscopy (TEM) results. In summary, nearly all of the data reported on the shock behavior of anhydrite is concluded from thermodynamic considerations or indirect observations. For that reason, we conducted six shock recovery experiments on anhydrite in the pressure range from 12.5 GPa up to 85 GPa. The aim of this study was to obtain an understanding of the shock behavior of anhydrite including deformation, transformation, and decomposition phenomena. Therefore, the recovered samples were investigated using X-ray diffraction and transmission electron microscopy.

METHODS

Experimental Setup

The recovery experiments were performed at the Ernst-Mach-Institut (EMI) on polycrystalline compact anhydrite discs with a diameter of 15 mm. The starting anhydrite rock is from the Upper Permian Zechstein mined in the potash works Sigmundshall at Bokeloh/Wunstorf, Germany. It is characterized by a random orientation of anhydrite grains with an average grain size of 200 μm. The experimental parameters used for obtaining pressures from 12.5 to 85 GPa are given in Table 1. The setup for the experiments consists of a high-explosive driven flyer plate, two steel blocks as momentum traps, and a cylindrical ARMCO-Fe container, in which the sample disc is embedded (Langenhorst and Deutsch 1994). Reverberation of the transmitted shock wave on the sample-container interfaces was used to reach peak-shock pressure. Pressures were calibrated as a function of cover and flyer plate thickness in separate experiments by pin contact measurements (see Langenhorst and Hornemann 2005). Optical microscopy revealed that samples shocked to pressures < 46.5 GPa are strongly fragmented powders, whereas above this pressure limit, samples are compact.

Analytical Methods

X-Ray Powder Diffraction

The X-ray powder diffraction patterns were obtained using a Stoe Stadi P X-ray diffractometer (BGI Bayreuth), equipped with a linear position-sensitive detector, a Co X-ray tube, and a primary Ge (111) monochromator. Si powder was added as standard reference material for lattice constant refinement. Peaks were fitted with a symmetric pseudo-Voigt profile-shape

function with FullProf (Rodríguez-Carvajal 1993). The crystal structure of anhydrite published by Hawthorne and Ferguson (1975) was used to model theoretic powder data with FullProf to assign the indices to the observed lines in diffraction patterns.

The cell refinement of anhydrite bears some complications, as two of the cell dimensions are very similar ($a \approx 6.993$ Å, $b \approx 6.995$ Å, and $c \approx 6.245$ Å in the *Amma* setting), resulting in overlapping peaks of similar indices *(hkl)* and *(khl)*. Therefore, these indices were omitted in the calculations. The unit-cell dimensions were refined by the program UnitCell (Holland and Redfern 1997) from peak positions of the 10 most intensive, nonoverlapping diffraction lines, i.e., (111), (012), (220), (212), (301), (103), (032), (232), (412), and (224) in the *Amma* setting.

X-ray line broadening was analyzed using the "double-Voigt" method (Balzar and Ledbetter 1993) which is based on the Warren–Averbach method (Warren and Averbach 1950; Warren 1959). The outcomes of the analysis are two domain size-related values and one strain-related value. The domain size-related values are calculated as mean surface weighted domain size and mean volume weighted domain size. There is no direct way of obtaining the actual strain, but it can be expressed as the root of the mean squared strain ($<\varepsilon^2(d)>^{1/2}$), which varies as a function of the chosen distance d. To obtain indicative values, half the surface or volume weighted domain size was chosen as representative distance. The original method of Warren (1959) was based on the investigation of related lattice planes such as (100), (200), and (300). Unfortunately, the diffraction pattern of anhydrite lacks these related lattice planes; hence, the regression was done through all the different, nonrelated (*hkl*) planes, and the results can therefore only be taken as average values in all directions.

Transmission Electron Microscopy

For TEM study, thin sections of 20–30 μm thickness were prepared from sample powder, glued on a copper grid of 3 mm in diameter, and thinned to perforation in an Ar-ion-milling system at 4.5 kV. After thinning and carbon coating, the thinned specimens were observed at 200 kV acceleration voltage using a Phillips CM20 STEM (BGI). Samples were investigated using conventional bright-field (BF) and dark-field (DF) imaging, as well as High-Resolution-TEM (HRTEM).

Dislocation densities were measured using the line intersection method (Hirsch et al. 1965), whenever possible. When dislocation density was too high, it was estimated using the surface intersection method (Hirsch et al. 1965) in a HRTEM image, whereby this dislocation density can only be considered as a minimum value.

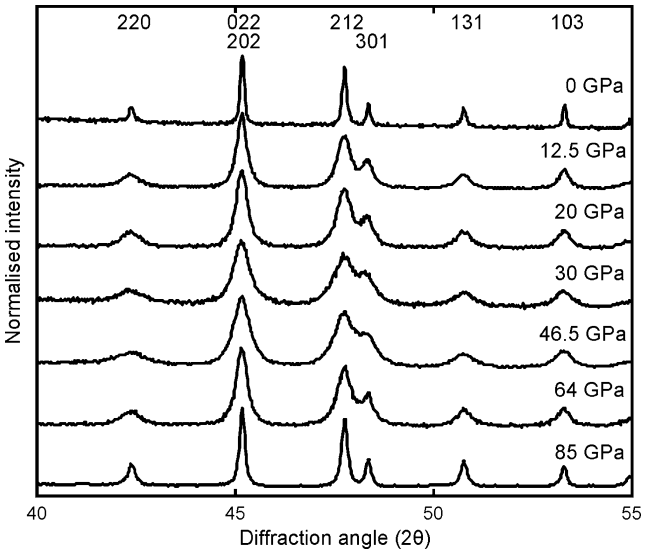

Fig. 1. X-ray diffraction patterns of unshocked and shocked anhydrite in a 2θ range from 40° to 55°. Intensities were normalized for comparison and (*hkl*) indices are shown above each peak.

RESULTS

X-Ray Diffraction Data

X-Ray Diffractograms

The X-ray diffraction patterns of unshocked and shocked anhydrite samples are summarized in Fig. 1. Unshocked anhydrite and the sample shocked at 85 GPa display sharp X-ray peaks, whereas the samples shocked to intermediate pressures (12.5, 20, 30, 46.5, and 64 GPa) show a marked broadening of X-ray lines due to limited crystallinity and strain. The observation of sharp X-ray peaks for the 85 GPa anhydrite suggests that postshock annealing has resulted in recovery of strain and enhancement of crystallinity. The peak positions of all shocked anhydrite samples are not significantly shifted in comparison to the unshocked reference sample, and detailed unit-cell refinement was required to reveal changes in lattice parameters.

Unit-Cell Parameters

Unit-cell parameters are presented in Fig. 2 as a function of pressure. The cell volume V increases up to a pressure of 33 GPa, followed by a continuous decrease in V with the pressure increasing to 46.5, 64, and 85 GPa. The values of V are lower than those of the 12.5 GPa sample. Within error limits, the cell volume at 85 GPa is equivalent to V of 305.48 Å^3 for unshocked anhydrite (Hawthorne and Ferguson 1975). Lattice constants a, b, and c show a less clear correlation with increasing pressure. The a and b constants seem to first slightly

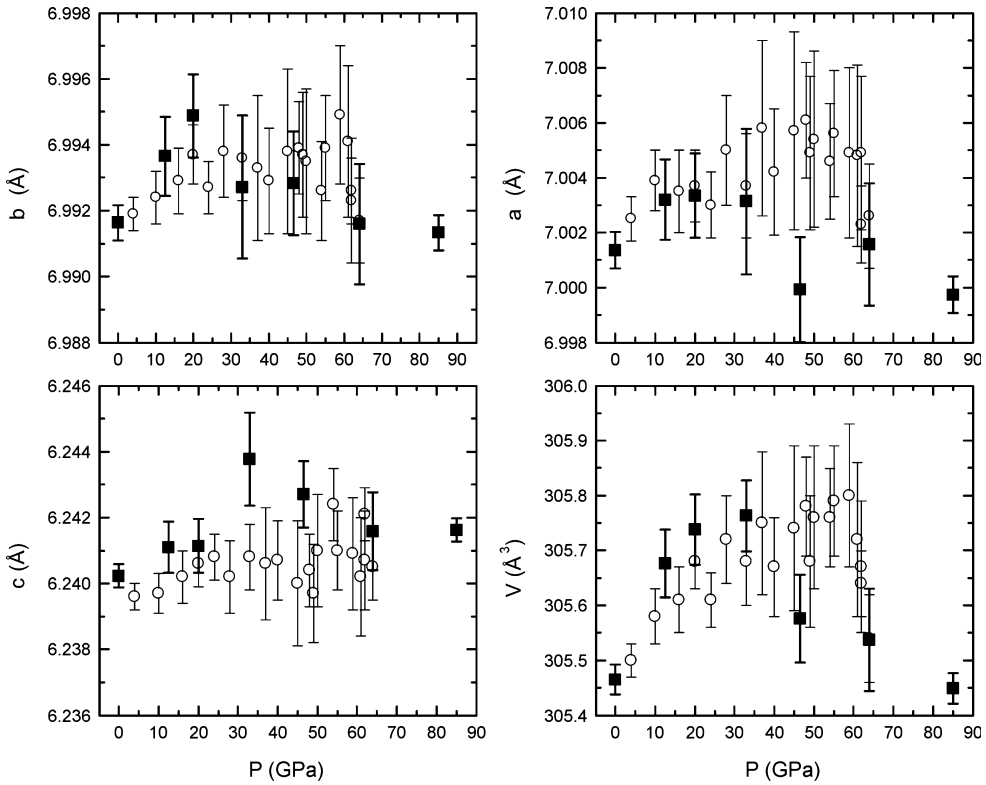

Fig. 2. Unit-cell dimensions of our experimentally shocked anhydrite (filled squares) compared with those (open circles) obtained by Skála et al. (2005). Error bars correspond to 1σ errors.

increase and then decrease with increasing pressure, whereas the *c* axis shows a slight increase with increasing pressure. However, it has to be considered that the errors are in the same order of magnitude as the variation of the parameters.

The variation in the unit-cell parameters of the shock-loaded anhydrite corresponds with less than 0.1% to the range of the variation reported by Skála et al. (2005) and Schmitt and Hornemann (1998). The data of Skála et al. (2005) also show that the unit-cell volume first increases, followed by a decrease with increasing shock pressure. However, the point of inflection at 60 GPa as observed by Skála et al. (2005) is distinctly higher than the 46.5 GPa observed in this study. The increase in unit-cell volume for the 20 GPa sample is largely due to the slight increase in the *a* lattice constant, whereas the unit-cell volume at 33 GPa increases due to the increase in the *c* lattice constant. The increase in the unit-cell volume is therefore not induced by the change in one specific lattice parameter.

Domain Size and Strain

Calculated volume and surface-weighted domain sizes are mean values that average over a heterogeneous size distribution. These mean domain sizes remain nearly constant up to 64 GPa, but a marked jump to high values occurs at 85 GPa (Figs. 3a and 3b). This is in accord with the data presented by Skála et al. (2005), who observed nearly constant domain sizes up to 64 GPa. Their data only reveal a small increase above 60 GPa, probably a first indication for an increasing domain size that finally results in the large domain size calculated from the X-ray diffraction line broadening in the present study.

The root mean square strain (RMSS) over the mean volume and mean size weighted domain sizes increase up to 46.5 GPa (Figs. 3c and 3d). At higher shock pressures, the RMSS decrease to reach finally at 85 GPa lower values than the sample shocked to 12.5 GPa. The RMSS variation observed here is also in agreement with the data of Skála et al. (2005). Their calculated RMSS increases up to approximately 40 GPa, remains nearly constant up to 50 GPa, and then decreases with increasing pressure.

TEM Observations

The TEM investigations reveal that the shocked anhydrite contains many different deformation effects, even at low pressures, and some decomposition features

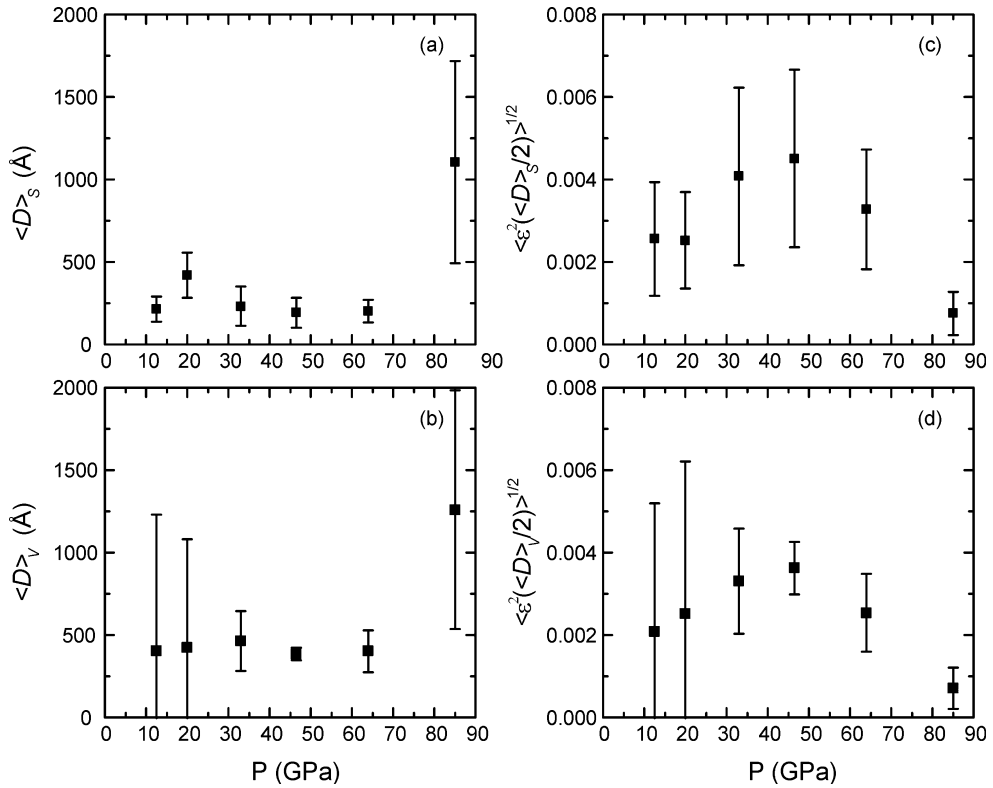

Fig. 3. Plots of (a) surface and (b) volume weighted domain size variation for the experimentally shocked anhydrite samples versus pressure. Changes in root mean square strain (RMSS) over surface and volume weighted domain sizes are shown in (c) and (d).

P (GPa)	12.5	20	33	46.5	64	85
corr. P (GPa)	7	14	22	30	41	55
twins	—				—	
sub-grains				—	—	—
increasing density and size of voids					—	—
dislocation density (m^{-2})	10^{13}	10^{14}	10^{16}	-	10^{13}	-

Fig. 4. Phenomena observed by TEM in the experimentally shocked anhydrite. The dislocation density of the 33 GPa sample was measured on a high-resolution (HR) TEM image, and represents a minimum value. Dislocation densities at 46.5 and 85 GPa could not be accurately measured because of heterogeneous distribution of dislocations.

at higher pressure. The observed phenomena are summarized in Fig. 4.

Dislocations and Planar Defects

Up to 20 GPa, anhydrite shows arrays of straight dislocations, twins, and sparsely distributed cracks (Fig. 5a). The traces of the dislocations can be indexed to lie in the (120), ($\bar{1}$20) and (020) planes and the twinning operation is a mirroring on the {210} planes (Fig. 5b).

The dislocation densities increase with increasing pressure from 10^{13} m^{-2} (12.5 GPa) to 10^{14} m^{-2} (20 GPa) up to 10^{16} m^{-2} at 33 GPa (Fig. 4). At 64 GPa, the dislocation density is again 10^{13} m^{-2}. In the samples shocked to 46.5 and 85 GPa, the distribution of dislocations was too heterogeneous to measure their density.

Multiple twinning occurs at 64 GPa with a twin different to that in the lower pressure regime (Fig. 6a): Twins are wedge- or lens-shaped, resembling ferro-elastic twins. In addition, planar defects parallel to the trace of (010) develop in the sample shocked to 64 GPa (Fig. 6b).

Sub-grains. At 46.5 GPa, small subgrains with sizes in the nm-range appear in high-resolution images (Fig. 7a). With increasing shock pressure, at 64 GPa (Fig. 7b), these subgrains gain a diameter of tens of nanometers, and are even visible in low resolution bright-field images at 85 GPa with a size in the μm-range.

Voids. A remarkably high density of voids occurs in the sample shocked at 64 GPa (Fig. 8a), whereby the voids are largest in the 85 GPa sample. Figure 8b shows a high-resolution image of a distorted structure next to a void in the 85 GPa sample. In addition, a channel of presumably newly formed grains extends from the void.

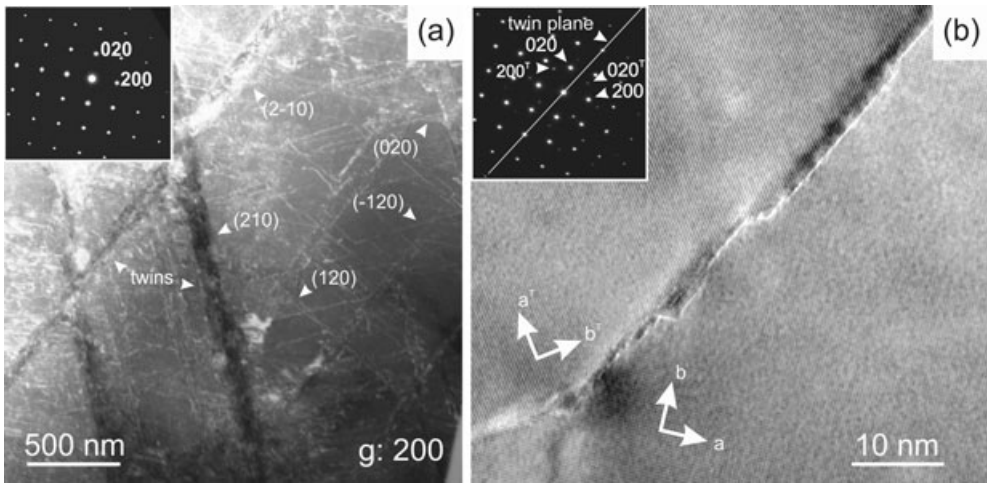

Fig. 5. Anhydrite sample 9460 shocked to 12.5 GPa; weak beam dark field (WBDF) image (a) showing dislocations, which can be indexed to lie in specific lattice planes, and multiple twinning; the HRTEM image (b) shows the twin plane.

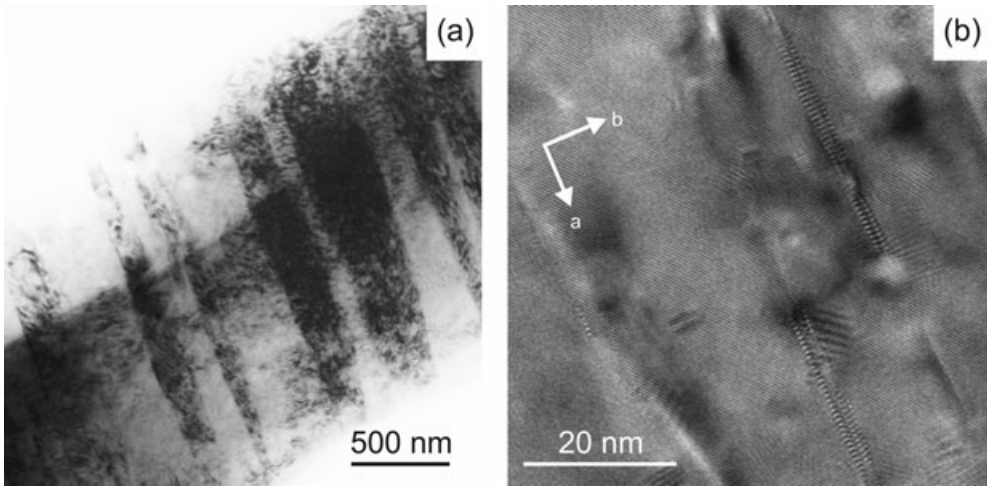

Fig. 6. Anhydrite sample 9456 shocked to 64 GPa; bright-field (BF) TEM image (a) showing multiple lens- and wedge-shaped twins. Their appearance resembles that of ferroelastic twins; (b) HRTEM image showing planar defects parallel to the trace of the (010) plane. These could be regarded as an indication for the anhydrite to monazite phase transition.

DISCUSSION

Microstructural Observations and Implications for the X-Ray Results

The observed phenomena in the TEM, summarized in Fig. 4, and the results of X-ray analysis are consistent with the physical parameters of the shock experiments. In the low pressure regime up to 20 GPa, shock and postshock temperatures and strain are relatively low; the samples react to these conditions by forming mechanical twins, which is a typical low temperature phenomena. The twinning planes (210) and $(2\bar{1}0)$ observed in this work do not agree with the twinning plane (011) reported by Ramez (1976a) for anhydrite deformed in static uniaxial pressure experiments between 0.1 and 0.5 GPa at temperatures up to 300 °C, indicating different twinning mechanisms due to different loading paths, dynamic, or static. The {120} twinning was observed so far only as contact twins in anhydrite (Anthony et al. 2003), but not as multiple twins such as those in our shock-loaded samples (Fig. 5a). However, typical mechanical twins have straight twin planes to their host crystals. The deformed twin planes observed here may be attributed to the very high stresses and/or multiple shocks resulting from the use of the reverberation technique.

Stress increases with higher shock pressure and therefore dislocation density and strain increases in the anhydrite samples shocked up to 33 GPa. The slip systems (010), [100], and {120} $[\bar{2}11]$ or $[\bar{2}\bar{1}1]$ as reported by Ramez (1976b) coincide well with the indices of the

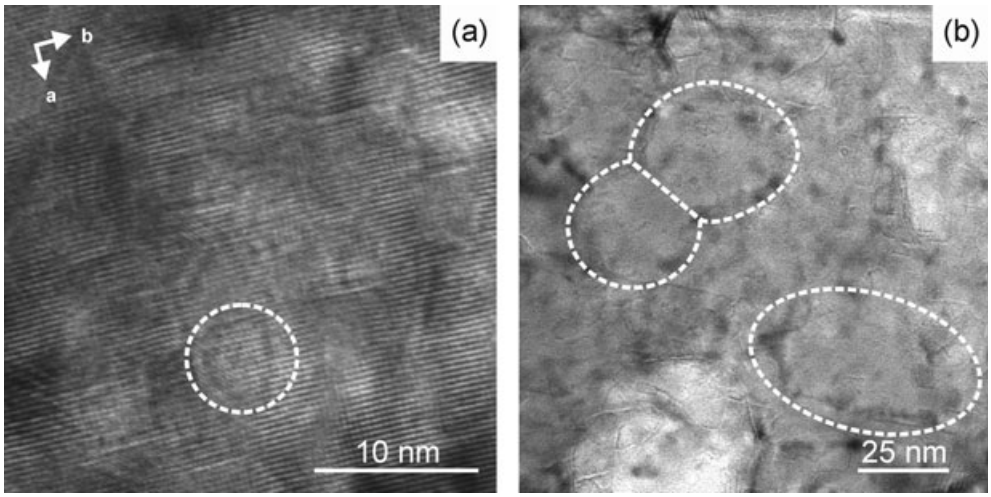

Fig. 7. HRTEM images of (a) anhydrite sample 9457 (46.5 GPa) and (b) anhydrite sample 9456 (64 GPa) showing subgrains formed by recrystallization. The subgrains become larger with increasing pressure. Dashed ellipses indicate the individual subgrains in both figures as a guide for the eye.

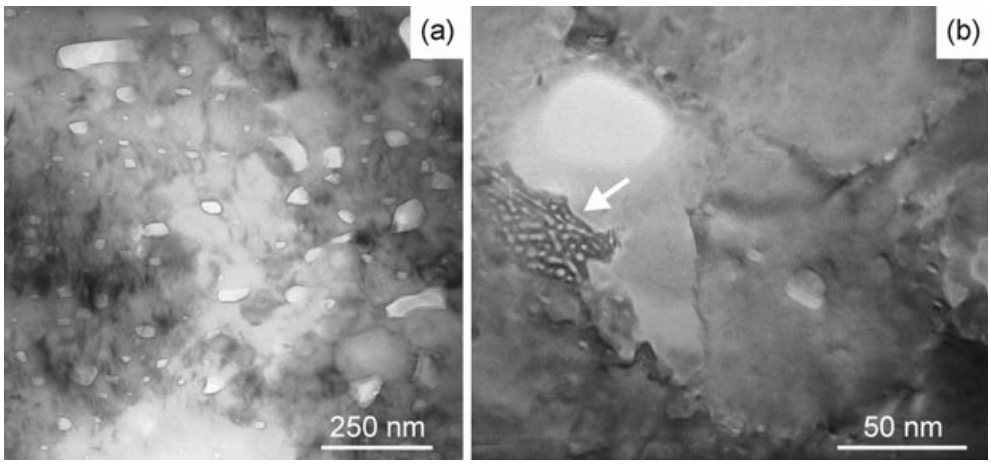

Fig. 8. a) Bright-field TEM image of anhydrite sample 9456 (64 GPa) illustrating the high density of voids, and b) HRTEM image showing the surroundings of a void (marked with an arrow) in anhydrite sample 9455, shocked to 85 GPa.

dislocation lines in the shock experiments at low pressures (Fig. 5a), indicating an identical or similar mechanism, despite the rate of deformation being different by several orders of magnitude. At 46.5 GPa, postshock temperatures are sufficient to initiate small-scale recovery due to annealing. Subgrains on the order of several nanometers in size start to form due to recrystallization of anhydrite to release the stress (Fig. 7a). However, the strain calculated from the X-ray diffraction patterns is still enhanced at this pressure, which may be related to the high dislocation density and the small size of the subgrains. At 85 GPa, the subgrains are very large (μm scale) and dislocations are rarely visible in the TEM. The decrease in strain and increase in domain size from 64 GPa to 85 GPa calculated from X-ray diffraction patterns is best explained by efficient annealing that causes a decrease in dislocation density and coarsening of subgrains.

Phase Transitions

Static in situ high-pressure studies on anhydrite have reported various phase transitions. Stephens (1964), Crichton et al. (2005), Ma et al. (2007), and Bradbury and Williams (2009) showed that anhydrite transforms between 2 and 5 GPa to a high-pressure phase with monoclinic monazite structure. This phase transition is unquenchable and the change in structure was proven by in situ X-ray and Raman measurements in a diamond anvil cell. Diamond anvil cell experiments performed at even higher pressures revealed further phase transitions: Crichton et al. (2005) reported a barite-type polymorph

at 21 GPa and 1450 °C and a quenched $AgMnO_4$ structure at 19.9 GPa, whereas Chen et al. (2001) found a conversion to a quenchable orthorhombic phase between 14 and 21 GPa. Furthermore, Raman measurements revealed a new phase at 33.2 GPa after laser heating (Ma et al. 2007). Moreover, the Hugoniot data of Simakov et al. (1974) provides evidence for a martensitic phase transition around 33 GPa upon shock loading. Bradbury and Williams (2009) concluded from kinetic calculations that the phase transition observed under shock loading around 33 GPa is the kinetically hampered phase transition observed in static experiments at 2–5 GPa; these authors also discarded the presence of any other phase transition upon 28 GPa reported in the above cited investigations.

Our TEM images of sample 9456 (64 GPa) provide hints at two different kinds of phase transformations in shock-loaded anhydrite, i.e., (1) a martensitic, and (2) a ferro-elastic phase transition.

1. The planar defects in Fig. 6b indicate an incipient martensitic phase transformation on the (010) planes in anhydrite. This may be assigned to the anhydrite-monazite transition. A structural model would be progressive shearing on the (010) planes (Fig. 9a) that leads to the zircon-type structure (Fig. 9b), followed by a distortion that deforms the lattice into the monazite-type structure (Fig. 9c). In the monazite structure, a ninth oxygen contributes to form AO_9 polyhedra, resulting in a structural distortion, specifically a rotation of the PO_4 tetrahedra and a lateral shift of the (100) plane.
2. The lens- and wedge-shaped appearance of the multiple twins in Fig. 6a indicates a ferro-elastic phase transition. This would imply a reversible displacive phase transition to a structural polymorph with higher symmetry. However, none of the above discussed phases into which anhydrite could transform possesses tetragonal or cubic symmetry. Further static high-pressure/high temperature experiments are needed to clarify the nature of this phase transition and stability of the new phase.

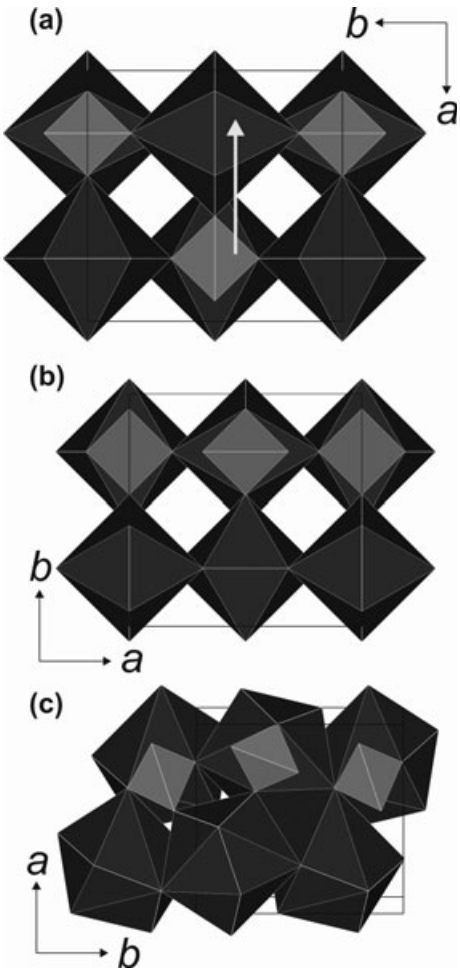

Fig. 9. Structural model of the semimartensitic anhydrite–monazite phase transition. Progressive shearing on the (010) planes (white arrow) in the anhydrite structure (a) leads to the zircon-type structure (b) and with increasing distortion deforms the lattice into the monazite structure (c).

SO_x Degassing

The large amount of voids and their increasing size in the pressure regime above 64 GPa indicates incipient decomposition of anhydrite despite the experimental set-up, which does not allow gas to expand significantly. These features provide evidence for high postshock temperatures. Figure 8b shows that pre-existing small cavities or fluid inclusions may constitute possible hot spots for decomposition. The temperature of the decomposition reaction $CaSO_4 \rightarrow CaO + SO_2 + \frac{1}{2}O_2$ is very close to the melting point of anhydrite at ambient conditions (Hanic et al. 1985). However, no decomposition products, melt features, or crystallization from melt have been observed in our experimentally shocked anhydrites. The closed container certainly inhibits release of SO_x gases which, if present, might back-react with the residual CaO.

Degassing of anhydrite in the context of an impact event is a process that occurs during decompression. The amount of gas released is only controlled by the postshock temperature and thus, by the energy difference between shock compression and release. Due to the multiple reflections in the reverberation method used in our experimental setup, the energy gain is lower than in a single (impedance) shock experiment or in a natural impact process. Due to these different loading paths, the threshold pressure of incipient degassing might be higher in our experiments than in nature. We estimated the different pressure loading steps by the multiple

reflections in the sample using Hugoniot data of ARMCO-FE (Bancroft et al.1956; Taylor and Rice 1963; Marsh 1980) and anhydrite (Simakov et al. 1974). The energy gain in the sample is given by:

$$\Delta E = E_R - E_S \quad (1)$$

where the Hugoniot energy of the reverberation experiment E_R depends on the shock pressure P and changes in volume V at every reverberation step:

$$E_R = \sum_i \frac{(P_i + P_{i-1})(V_{i-1} - V_i)}{2} \quad (2)$$

and the isentropic energy E_S depends on relative volume change:

$$E_S = -\int_{V_0}^{V_H} P_S \mathrm{d}V \quad (3)$$

where P_s is the pressure at the isentrope corresponding to the final specific volume V_H. The analytical form assumed for the isentrope is the Birch–Murnaghan equation of state:

$$P_S = \frac{3K_0}{2}\left[\left(\frac{V_0}{V_H}\right)^{7/3} - \left(\frac{V_0}{V_H}\right)^{5/3}\right] \left\{1 + \frac{3}{4}(K_0 - 4)\left[\left(\frac{V_0}{V_H}\right)^{2/3} - 1\right]\right\} \quad (4)$$

where K_0 and K'_0 are the isentropic bulk modulus and its isentropic pressure derivative. V_0 is the initial specific volume. To keep calculations simple, we do not take into account any phase changes in anhydrite. The maximum relative error in ΔE by neglecting the anhydrite–monazite phase transition reported by Simakov et al. (1974) will be 10% (Ivanov et al. 1996), which is in the range of the accuracy of the computation. The energy gained in our reverberation experiments can be converted into a corresponding impedance shock pressure that is needed to result in the same energy increase. In impedance experiments, the shock pressures are reached in one step. Thus, the impedance Hugoniot energy E_H can be calculated as:

$$E_H = \frac{1}{2} P_H (V_0 - V_H) \quad (5)$$

The energy gain in the sample is again the difference between the Hugoniot energy E_H and the isentropic energy E_s of the release path. Table 2 lists the reverberation and impedance shock pressures that would result in equivalent energy gain. Our calculations indicate that in a natural impact incipient degassing from nonporous anhydrite would start between 30 and 41 GPa, in good accordance with the threshold pressure of 32.5 GPa given by Gupta et al. (2001).

Table 2. Conversion of nominal shock pressure in reverberation shock experiments performed with anhydrite powder to the nominal pressure in impedance shock experiments with the identical gain in energy (see text for further explanation).

Experiment	Reverberation pressure (GPa)	Impedance pressure (GPa)
9460	12	7
9459	20	14
9458	33	22
9457	46.5	30
9456	64	41
9455	85	55

See text for further explanation.

The maximum energy gain in our reverberation experiments at 85 GPa is comparable to the gain in a shock impedance experiment at 55 GPa, well below the predicted melting of shock-loaded anhydrite in the pressure range of 80–90 GPa by Ivanov et al. (2004). This is in accordance with the lack of indications for any melting of anhydrite in our samples. In the case of calcite-quartz-gypsum mixtures also shocked with the reverberation technique, however, Bell (2010) documented features characteristic for melting of the hydrated sulfate already in the 24 GPa experiment. We tentatively conclude that not only the porosity of the target materials but also the presence of water may lower the threshold for melting and dissociation.

CONCLUSION

Six shock experiments on anhydrite powder were conducted with the reverberation technique at nominal peak-shock pressures of 12.5, 20, 33, 46.5, 64, and 85 GPa, respectively. The samples were investigated using X-ray powder diffraction and TEM. The recovered anhydrite shows a number of shock effects such as formation of twins, dislocations, and voids, as well as polygonization. These effects could be potential pressure indicators in unaltered impact breccias from natural craters. Their occurrence in certain pressure ranges is summarized in Fig. 4.

In the lower pressure regime up to 20 GPa, the recovered samples show mainly "cold" deformation phenomena such as cracks and deformation twins. The dislocation density increases up to 33 GPa, and the strain increases up to 46.5 GPa. In the pressure range from 46.5 to 85 GPa, the postshock temperatures are high enough to anneal the deformation features. The anhydrite recrystallizes, whereby the dislocation density

decreases. This results in the formation of subgrains with their size increasing with increasing shock pressure.

The increase in the density and size of voids in the anhydrite samples shock-loaded to 64 and 85 GPa suggests partial decomposition of anhydrite. Only high postshock temperature triggers this phenomenon, but due to the loading path that is very different in our reverberation shock experiments compared with nature, the shock pressures have to be adjusted to the natural loading path. These calculations resulted in the onset of degassing of anhydrite in the pressure range of 30–41 GPa. However, no decomposition products, melts, or grains crystallized from a melt were observed over the whole pressure range investigated. In natural impacts, the solid residue of decomposition may either back-react with gas to form anhydrite or be incorporated in hot silicate melts. The best example for the latter process is provided by the K-Pg ejecta deposit at Beloc, Haiti, that contains "dry" yellow silicate glasses with high CaO contents (approximately 25 wt% CaO), and up to 1 wt% SO_3 (e.g., Sigurdsson et al. 1992). Anhydrite, however, is virtually absent in K-Pg ejecta deposits (e.g., Schulte et al. 2010). However, this fact cannot be used as an argument for complete degassing of the anhydrite layers at the Chicxulub target site, as anhydrite is known to be easily converted into gypsum which, in turn, is soluble during diagenesis and alteration.

Acknowledgments—We are grateful for financial support provided by the Deutsche Forschungsgemeinschaft (DFG LA 830/4-4, LA 830/14-1, DE 401/15-4, HO 1446/3-4). We appreciate the skilled technical assistance by Michael Feldhaus (Münster), and very interesting discussions with Boris Ivanov (Moscow). We thank F. Hörz and H. Leroux for their constructive reviews.

Editorial Handling—Dr. Uwe Reimold

REFERENCES

Agrinier P., Deutsch A., Schärer U., and Martinez I. 2001. Fast back-reactions of shock-released CO_2 from carbonates: An experimental approach. *Geochimica et Cosmochimica Acta* 65:2615–2632.

Anthony J. W., Bideaux R. A., Bladh K. W., and Nichols M. C. 2003. *Handbook of mineralogy, Volume V. Borates, carbonates, sulfates*. Tucson, AZ: Mineral Data Publishing. 813 p.

Badjukov D. D., Dikov Y. P., Petrova T. L., and Pershin S. V. 1995. Shock behavior of calcite, anhydrite, and gypsum (abstract). 26th Lunar and Planetary Science Conference. pp. 63–64.

Balzar D. and Ledbetter H. 1993. Voigt modeling in Fourier analysis of size- and strain-broadened X-ray diffraction peaks. *Journal of Applied Crystallography* 26:97–103.

Bancroft D., Peterson E. L., and Minshall S. 1956. Polymorphism of iron at high pressure. *Journal of Applied Physics* 27:291–298.

Bell M. S. 2010. Relative shock effects in mixed powders of calcite, gypsum, and quartz: A calibration scheme from shock experiments. In *Large meteorite impacts and planetary evolution IV*, edited by Gibs L. and Reimold W. U. GSA Special Paper 465. Boulder, Colorado: Geological Society of America. pp. 125–139.

Bradbury S. E. and Williams Q. 2009. X-ray diffraction and infrared spectroscopy of monazite-structured $CaSO_4$ at high pressures: Implications for shocked anhydrite. *Journal of Physics and Chemistry of Solids* 70L:134–141.

Chen C. C., Liu L. G., Lin C. C., and Yang Y. J. 2001. High-pressure phase transformation in $CaSO_4$. *Journal of Physics and Chemistry of Solids* 62:1293–1298.

Chen G., Tyburczy J. A., and Ahrens T. J. 1994. Shock-induced devolatilization of calcium sulfate and implications for K-T extinctions. *Earth and Planetary Science Letters* 128:615–628.

Crichton W. A., Parise J. B., Sytle M. A., and Grzechnik A. 2005. Evidence for monazite-, barite-, and $AgMnO_4$ (distorted barite)-type structures of $CaSO_4$ at high pressure and temperature. *American Mineralogist* 90:22–27.

Deutsch A. and Langenhorst F. 2007. On the fate of carbonates and anhydrite in impact processes – evidence from the Chicxulub event. *GFF [Geologiska Föreningens I Stockholm Förhandlingar]* 129:155–160.

Gupta S. C., Ahrens T. J., and Yang W. 2001. Shock-induced vaporization of anhydrite and global cooling from the K/T impact. *Earth and Planetary Science Letters* 188:399–412.

Hanic F., Galikova L., Havlica J., Kapralik I., and Ambruz V. 1985. Kinetics of the thermal decomposition of $CaSO_4$ in air. *Transactions & Journal of the British Ceramic Society* 84:22–25.

Hawthorne F. C. and Ferguson R. B. 1975. Anhydrous sulfates II. Refinement of the crystal structure of anhydrite. *Canadian Mineralogist* 13:289–292.

Hirsch P. B., Howie A., Nicholson R. B., Pashley D. W., and Whelan M. J. 1965. *Electron microscopy of thin crystals*. London: Butterworths. 549 p.

Holland T. J. B. and Redfern S. A. T. 1997. Unit cell refinement from powder diffraction data: The use of regression diagnostics. *Mineralogical Magazine* 61:65–77.

Ivanov B. A. and Deutsch A. 2002. The phase diagram of $CaCO_3$ in relation to shock compression and decomposition. *Physics of the Earth and Planetary Interiors* 129:131–143.

Ivanov B. A., Badukov D. D., Yakovlev O. L., Gerasimov M. V., Dikov Y. P., Pope K. O., and Ocampo A. C. 1996. Degassing of sedimentary rocks due to Chicxulub impact: Hydrocode and physical simulations. In *The cretaceous-tertiary event and other catastrophes in earth history*, edited by Ryder G., Fastovsky D. E., and Gartner S. GSA Special Paper 307. Boulder, Colorado: Geological Society of America. pp. 125–139.

Ivanov B. A., Langenhorst F., Deutsch A., and Hornemann U. 2002. How strong was impact-induced CO_2 degassing in the K/T event? Numerical modeling of laboratory experiments. In *Catastrophic events and mass extinctions: Impacts and beyond*, edited by Koeberl C. and Macleod K. G. GSA Special Paper 356. Boulder, Colorado: Geological Society of America. pp. 587–594.

Ivanov B. A., Langenhorst F., Deutsch A., and Hornemann U. 2004. Anhydrite EOS and phase diagram in relation to shock decomposition (abstract #1489). 35th Lunar and Planetary Science Conference. CD-ROM.

Kondo K.-I. and Ahrens T. J. 1983. Heterogeneous shock-induced thermal radiation in minerals. *Physics and Chemistry of Minerals* 9:173–181.

Kring D. A. 2007. The Chicxulub impact event and its environmental consequences at the Cretaceous-Tertiary boundary. *Palaeogeography, Palaeoclimatology, Palaeoecology* 255:4–21.

Langenhorst F. and Deutsch A. 1994. Shock experiments on pre-heated α- and β-quartz: 1. Optical and density data. *Earth and Planetary Science Letters* 125:407–420.

Langenhorst F. and Hornemann U. 2005. Shock experiments on minerals: Basic physics and techniques. In *EMU notes in mineralogy: Mineral behaviour at extreme conditions*, edited by Miletich R. vol. 7, Chapter 15. Budapest: Eötvös University Press. pp. 357–387.

Langenhorst F., Boustie M., Deutsch A., Hornemann U., Matignon Ch., Migault A., and Romain J. P. 2002. Experimental techniques for the simulation of shock metamorphism. A case study on calcite. In *High-pressure shock compression of solids V—Shock chemistry and meteoritic applications*, edited by Davison L., Horie Y., and Sekine T. Berlin, Heidelberg, New York: Springer. pp. 1–27.

Langenhorst F., Deutsch A., Hornemann U., Ivanov B. A., and Lounejeva E. 2003. On the shock behaviour of anhydrite: Experimental results and natural observations (abstract #1638). 34th Lunar and Planetary Science Conference. CD-ROM.

Ma Y. M., Zhou Q., He Z., Li F. F., Yang K. F., Cui Q. L., and Zou G. T. 2007. High-pressure and high-temperature study of the phase transition in anhydrite. *Journal of Physics: Condensed Matter* 19: 425221.

Marsh L. 1980. *LASL shock hugoniot data*. Berkeley, California: University of California Press. 658 p.

Ohno S., Kadono T., Kurasosawa K., Sakaiya T., Sugita S., Shigemori K., Hironaka Y., Watari T., and Matsui T. 2010. Experimental study of SO_2/SO_3 ratio in impact vapor plumes using a high-speed laser gun: Initial results (abstract). *Earth and Planetary Science Congress* 5:2010-184.

Osinski G. R. and Spray J. G. 2001. Impact-generated carbonate melts: Evidence from the Haughton structure, Canada. *Earth and Planetary Science Letters* 194:17–29.

Pierazzo E., Hahmann A. N., and Sloan L. C. 2003. Chicxulub and climate: Radiative perturbations of impact-produced S-bearing gases. *Astrobiology* 3:99–118.

Pope K. O., Baines K. H., Ocampo A. C., and Ivanov B. A. 1997. Energy, volatile production, and climatic effects of the Chicxulub Cretaceous/Tertiary impact. *Journal of Geophysical Research* 102:21645–21664.

Ramez M. R. H. 1976a. Mechanisms of intergranular gliding in experimentally deformed anhydrite. *Neues Jahrbuch Mineralogie Abhandlungen* 127:311–329.

Ramez M. R. H. 1976b. Fabric changes in experimentally deformed anhydrite rocks. *Neues Jahrbuch Mineralogie Abhandlungen* 128:89–113.

Rodríguez-Carvajal J. 1993. Recent advances in magnetic structure determination by neutron powder diffraction. *Physica B* 192:55–69.

Schmitt R. T. and Hornemann U. 1998. Shock experiments with a natural anhydrite-quartz-sample (abstract #1019). 29th Lunar and Planetary Science Conference. CD-ROM.

Schulte P., Alegret L., Arenillas I., Arz J. A., Barton P. J., Bown P. R., Bralower T. J., Christeson G. L., Claeys P., Cockell C. S., Collins G. S., Deutsch A., Goldin T. J., Goto K., Grajales-Nishimura J. M., Grieve R. A. F., Gulick S. P. S., Johnson K. R., Kiessling W., Koeberl C., Kring D. A., Macleod K. G., Matsui T., Melosh J., Montanari A., Morgan J. V., Neal C. R., Nichols D. J., Norris R. D., Pierazzo E., Ravizza G., Rebolledo-Vieyra M., Reimold W. U., Robin E., Salge T., Speijer R. P., Sweet A. R., Urrutia-Fucugauchi J., Vajda V., Whalen M. T., and Willumsen P. S. 2010. The Chicxulub impact and mass extinction at the Cretaceous–Paleogene boundary. *Science* 327:1214–1218.

Sigurdsson H., D'Hondt S., and Carey S. 1992. The impact of the Cretaceous/Tertiary bolide on evaporate terrane and generation of major sulfuric acid aerosol. *Earth and Planetary Science Letters* 109:543–559.

Simakov G. V., Pavlovskiy M. N., Kalashnikov N. G., and Trunin R. F. 1974. Udarnaya szhimaemost' dvenadtsati mineralov [Shock compressibility of twelve minerals]. Izvestiya AN SSSR, *Fizika Zemli* 8:543–560.

Skála R., Langenhorst F., and Hörz F. 2004. Assessing the role of anhydrite in the KT mass extinction: Hints from shock-loading experiments (abstract #1284). 35th Lunar and Planetary Science Conference. CD-ROM.

Skála R., Hörz F. P., and Langenhorst F. 2005. Experimentally shock-loaded anhydrite: Unit-cell dimensions, microstrain and domain size from X-ray powder diffraction. In *Large meteorite impacts III*, edited by Kenkmann T., Hörz F., and Deutsch A. GSA Special Paper 384. Boulder, Colorado: Geological Society of America. pp. 413–426.

Stephens D. R. 1964. The hydrostatic compression of eight rocks. *Journal of Geophysical Research* 69:2967–2978.

Taylor J. W. and Rice M. H. 1963. Elastic-plastic properties of iron. *Journal of Applied Physics* 34:364–371.

Warren B. E. 1959. X-ray studies of deformed metals. *Progress in Metal Physics* 8:147–202.

Warren B. E. and Averbach B. L. 1950. The effect of cold-work distortion on X-ray patterns. *Journal of Applied Physics* 21:595–599.

Wiseman S. M., Arvidson R. E., Morris R. V., Poulet F., Andrews-Hanna J. C., Bishop J. L., Murchie S. L., Seelos F. P., Des Marais D., and Griffes J. L. 2010. Spectral and stratigraphic mapping of hydrated sulfate and phyllosilicate-bearing deposits in northern Sinus Meridiani, Mars. *Journal of Geophysical Research* 115: E12, CiteID E00D18.

Wünnemann K., Collins G. S., and Osinski G. R. 2008. Numerical modelling of impact melt production in porous rocks. *Earth and Planetary Science Letters* 269:530–539.

Yang W. and Ahrens T. J. 1998. Shock vaporization of anhydrite and global effects of the K/T bolide. *Earth and Planetary Science Letters* 156:125–140.

Zel'dovich Y. B. and Raizer Y. P. 2002. *Physics of shock waves and high-temperature hydrodynamic phenomena*. Mineola, NY: Dover Publication, 916 p.

Zhang F. and Sekine T. 2007. Impact-shock behavior of Mg- and Ca-sulfates and their hydrates. *Geochimica et Cosmochimica Acta* 71:4125–4133.